Unlocking the intermediate-phase evolution in perovskite crystallization with an operando infrared FEWS sensor

Mingquan Liao, Yongkun Zhao, Yinsheng Xu, Guoping Dong, Xianghua Zhang, Guangda Niu, Mengling Xia

Unlocking the intermediate-phase evolution in perovskite crystallization with operando infrared FEWS sensor

MINGQUAN LIAO,[1] YONGKUN ZHAO,[1] YINSHENG XU,[1,*] GUOPING DONG,[2] XIANGHUA ZHANG[1,3] GUANGDA NIU,[4] MENGLING XIA,[1,*]

[1]*School of Materials Science and Engineering & State Key Laboratory of Silicate Materials for Architectures, Wuhan University of Technology, Wuhan 430070, China.*

[2]*State Key Laboratory of Luminescent Materials and Devices, South China University of Technology, Guangzhou 510640, China.*

[3]*Institut des Sciences Chimiques de Rennes - UMR CNRS 6226, Université de Rennes, Rennes 35042, France.*

[4]*Wuhan National Laboratory for Optoelectronics, Huazhong University of Science and Technology, Wuhan 430074, China.*

*Corresponding authors: xuyinsheng@whut.edu.cn (Y. Xu), xiamengling@whut.edu.cn (M. Xia).

Received XX Month XXXX; revised XX Month, XXXX; accepted XX Month XXXX; posted XX Month XXXX (Doc. ID XXXXX); published XX Month XXXX

The intermediate-phase produced by the complexation of metal ions and solvent molecules usually occurred in the crystallization process of perovskite single crystal or film. Effective in-situ monitoring of intermediate-phase evolution is beneficial to the control of crystal quality. However, it is difficult to realize. In this work, infrared fiber evanescent wave spectroscopy (FEWS) was raised to monitor the intermediate-phase evolution in real-time and non-destructively using GeAsSeTe chalcogenide optical fibers. The vibrational and rotational dynamics of specific molecular functional groups was operando captured, reflecting perovskite precursor of different states. Taking BM_2PbBr_4 (BM=benzimidazole) perovskite as an example, the shift of the stretching vibration of -C=O groups in DMF (N,N-Dimethylformamide) towards low-wavenumbers and then recovered towards original position probed the complexion of Pb^{2+} and carbonyl groups into $(DMF)_2BMPbBr_3$ intermediate-phase and then decomplexing to precipitate BM_2PbBr_4 perovskite crystal. Some anomalous emergence of new vibrational bands associating with -C-N and -N-H bonds suggest the variation of DMF-BMBr hydrogen bonds during intermediate-phase evolution. This technique provides new insights into the control of perovskite crystallization processes, and pushes the development of high-quality perovskite materials for high-performance photovoltaic or optoelectronic devices.

https://doi.org/××××/OL. ××××××

Recently, metal halide perovskites have emerged as prominent materials in the realm of optoelectronic applications, such as photovoltaics, photodetectors, and light-emitting diodes.[1-4] Their optoelectronic performance is highly reliant on the quality of the material itself. For instance, the crystallization quality of perovskite films directly impacts the photoelectric conversion efficiency in perovskite solar cells.[5] Similarly, the quality of perovskite single crystal dictates its detection efficiency as a photodetector.[6,7] Specifically, poor crystal quality means more defects in perovskite materials, potentially leading to undesirable non-radiative carrier or exciton recombination, thereby affecting device performance.[8,9]

Given the profound influence of the nucleation and growth on crystallization quality of perovskite crystals, numerous strategies have been devised to manipulate nucleation sites and growth rates.[10-12] One notable approach is solvent coordination engineering. For example, the formation of the MAI-PbI_2-DMSO coordination intermediate phase, followed by gradual dissociation of coordination, plays a pivotal role in the crystallization process of $MAPbI_3$ polycrystalline films in perovskite solar cells.[13,14] As chemical reactions involved in coordination and dissociation processes are dynamic, they are subject to multi-parameter disturbances, which often dictate crystallization quality. Consequently, monitoring the evolution of intermediate-phases is essential for comprehending and regulating the perovskite crystallization process.

Previously reported operando techniques for perovskites include X-ray-based probes (e.g., GIWAXS, XPS, EXAFS, *etc.*),[13,15-17] electron-based probes (e.g., TEM, SEM, *etc.*),[16,18] and UV/visible/infrared probes (e.g., TAS, FTIR, PL, *etc.*).[19-21] In situ GIWAXS has emerged as a widely recognized and effective method for characterizing the crystallization process of perovskite.[22] However, these methods rely on intricate and expensive laboratory equipment, rendering them impractical for routine monitoring of intermediate-phase evolution for real-time assessment of perovskite crystallization.[23,24] Consequently, there is a pressing need to develop non-invasive monitoring tools and analytical methods (compatible with perovskite precursors) capable of unveiling intermediate-phase evolution and elucidating factors influencing perovskite crystal quality.

Non-destructive diagnostic techniques, such as optical sensing, enable real-time characterization with spatial resolution achieved by embedding sensors directly within the target solution.[25,26] Optical fiber Bragg grating (FBG) sensors allow for the measurement of various parameters, including temperature and strain.[27-29] Additionally, tilted FBG sensors offer the potential to access refractive index and turbidity by capturing the interaction between

the fiber-guided light and its local environment, thereby providing insights into molecular processes occurring during intermediate-phase evolution.[30] By integrating fibers with IR spectra, fiber-based IR spectroscopy can accurately capture the vibrational and rotational dynamics of specific molecular functional groups in an operando manner.[31,32] Chalcogenide glass optical fibers feature transmission windows ranging from 2 to 13 μm, significantly broader than those of conventional silica optical fibers (0.8~2 μm), thus expanding the range of detectable molecules.[33] However, the real-time monitoring of intermediate-phase evolution during perovskite crystallization via fiber-based IR spectroscopy remains largely unexplored.

Herein, we introduce the application of IR fiber evanescent wave spectroscopy (FEWS) to monitor the intermediate-phase evolution in perovskite precursor solutions. By employing GeAsSeTe (GAST) optical fibers, characterized by broad infrared transmission ranges and high stability, we achieved precise characterization of infrared absorption features within perovskite precursor solutions of different states. The shift of the stretching vibration of -C=O groups from 1655 cm^{-1} to 1639 cm^{-1} and then recovered towards original position indicated the complexion of Pb^{2+} and carbonyl groups into $(DMF)_2BMPbBr_3$ intermediate-phase and then decomplexing to precipitate BM_2PbBr_4 perovskite crystal. The operando monitoring of the variation of DMF- BMBr hydrogen bonds also supported the intermediate- phase evolution mechanism. This real-time, non-destructive monitoring approach revealed distinct spectral changes across different compositions, offering valuable insights into the control of perovskite crystallization processes. The sensor demonstrates promising potential for real-time monitoring during the production of perovskite materials for high-performance photovoltaic or optoelectronic devices.

Fig. 1a depicts the experimental arrangement for real-time monitoring of perovskite precursors using fiber-based IR spectroscopy. The GAST fiber was directly immersed into the solution. Mid-infrared light in the wavelength range of 2.5 to 25 μm propagated through the GAST fiber core via total internal reflection. This fiber-guided light interacted with the local environment, generating an evanescent wave at the fiber surface (**Fig. 1b**). IR spectroscopy leverages evanescent waves to probe molecular species at the fiber surface over a specific distance. In contrast to conventional attenuated total reflection (ATR) techniques,[34] which involve limited total internal reflections, the utilization of multiple evanescent waves interacting with the local environment significantly enhances the sensitivity of detecting molecules (**Fig. 1b**). The variation in the coordination state of molecules reflects the essence of intermediate-phase evolution during perovskite crystallization **(Fig. 1c**). This alteration in molecular dipole moment enables the recognition of molecular species.

As a proof of concept, the GAST optical fiber was guided through a liquid cell without contacting the inner wall. The specific parameters and loss spectra of the GAST optical fiber are presented in **Fig. S1** and **S2**. Operando IR spectra were collected both before and after solution injection, as depicted in **Fig. 2a**. The acquisition commenced with an empty cell, resulting in no discernible absorbance owing to the absence of solution molecules. Then every 30 min intervals, different solutions were sequentially introduced in the following order: a small volume of DMF, 3 M BM in DMF, and 1 M $PbBr_2$ in DMF. Concurrent with their injection into the liquid cell, IR bands characteristic of DMF, BM/DMF, and $PbBr_2$/DMF emerged, respectively, consistent with reference spectra of identical solutions obtained via ATR spectroscopy (**Fig. 2b**). Noted that $PbBr_2$ dissolved in DMF tends to complex with C=O bond of DMF, which makes the vibration band of C=O band move to low wavenumber (**Fig. 2a**). Additionally, the sensitivity and limit of detection (LOD) of the GAST optical fiber sensor were evaluated, revealing that the LOD for BM in DMF is below 0.46 $mmol \cdot mL^{-1}$. (**Fig. S3** and **Table S1**).

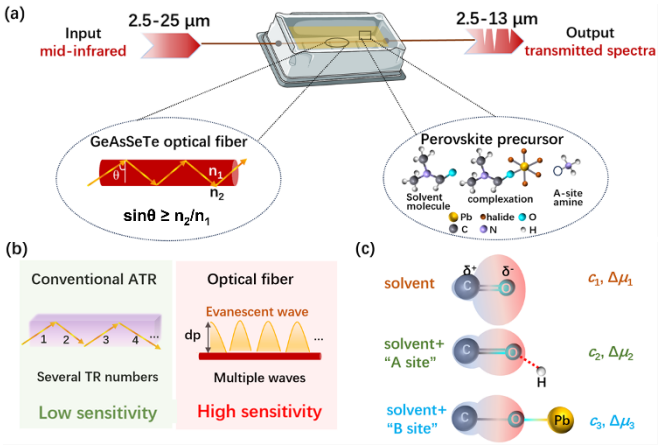

Fig. 1. (a) Schematic of GAST chalcogenide fiber into perovskite precursor solution and real-time monitoring of molecular changes in perovskite precursors. (b) Comparison of conventional ATR inside the fiber and evanescent wave created at the fiber surface. (c) Different coordination states of solvent molecules result in the change of molecular dipole moment (μ).

Perovskite crystallization begins when the concentration of the solution exceeds the saturation solubility due to solvent evaporation. The ultimate product targeted is BM_2PbBr_4, characterized by a layered crystal structure, as depicted in **Fig. S4**. The crystallization process of BM_2PbBr_4 is usually accompanied by the formation and decomposition of $(DMF)_2BMPbBr_3$ intermediate-phase with one-dimensional crystal structure[35]. Monitoring of the crystallization process was conducted using GAST optical fiber. Microscopic examination revealed no noticeable corrosion on the surface of our GAST fiber after 48 h of immersion in the perovskite precursor solution (**Fig. S5**). The absorbance of optical fibers in common solvents (DMF, DMSO, and GBL) used for perovskite dissolution exhibited negligible variation over time (**Fig. S6**). Additionally, the absorbance of fibers was assessed at different temperatures (**Fig. S7**). A temperature change of 10 °C yielded an infrared absorbance change of less than 1%, with band position displacement falling below the spectrometer resolution. This further validates the suitability of GAST fiber for in-situ monitoring of perovskite crystallization by manipulating temperature to reduce saturation solubility. The aforementioned experiments collectively demonstrate that GAST fiber remains unaffected by the surrounding environment during the detection of intermediate-phase evolution.

The crystal configuration was analyzed using single-crystal XRD diffraction, and simplified schematic representations of the resolved structures are provided in **Fig. 3a** and **S8a**. For the purpose of tracking the intermediate-phase evolution, IR-FEWS absorbance

spectra were systematically recorded from the initiation of complexation to the completion of decomplexation (**Fig. 3b**). The acquisition frequency for IR-FEWS absorbance spectra was set as 32 scans per minute, with a resolution of 4 cm^{-1}. For comparison, absorbance spectra were also recorded on the crystallization without the formation of intermediate-phase by the direct interacting between $PbBr_2$ and BMBr (**Fig. S8b**). The absence of intermediate-phase products was ensured by introducing excess BMBr to impede the formation of $(DMF)_2BMPbBr_3$ intermediate-phase, according to $BMBr + BMPbBr_3 \Leftrightarrow BM_2PbBr_4$. As depicted in **Fig. 3b** and **S8b**, we have marked the attribution of different vibration bands.

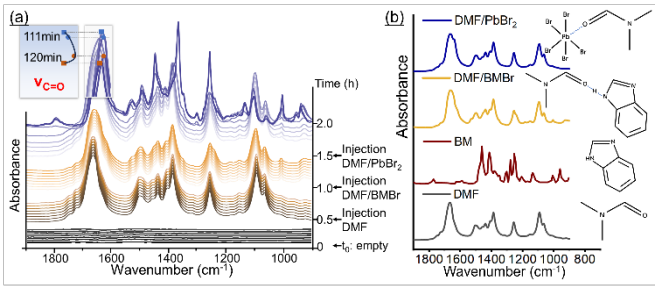

Fig. 2. (a) IR-FEWS absorbance spectra as a function of time, with injection of different solution into the liquid cell. (b) Reference ATR-FTIR absorbance spectra of the different solutions injected during the experiment. The inset is the molecular configuration.

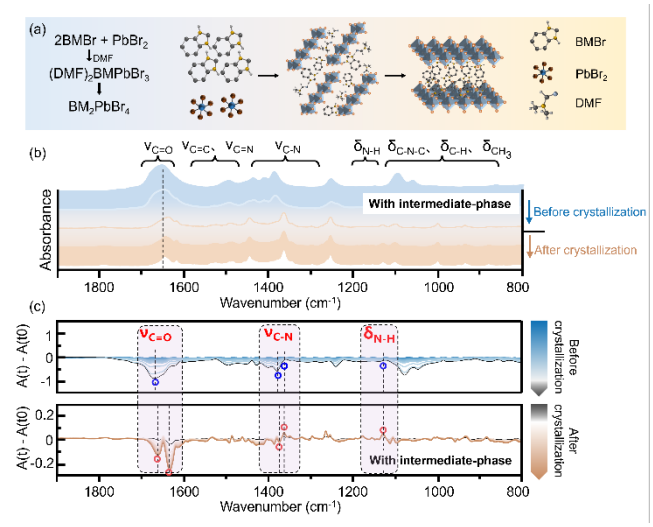

Fig. 3. (a) Schematic illustration of the perovskite crystallization process during the formation of the intermediate phase. (b) Operando IR-FEWS spectra collected during the perovskite crystallization, with spectral colors transitioning from blue (before crystallization) to yellow (after crystallization). (c) Evolution of the relative absorbance, $A(t)$-$A(t_0)$, before and after crystallization. The relative positions of the absorbance bands are indicated with dashed lines and annotated with circular markers.

Fig. 3c illustrates the relative absorbance evolution corresponding to IR-FEWS absorption spectra during complexing (blue) and decomplexing (yellow). The relative absorbance for various vibration bands is determined by the calculation $A(t)$-$A(t_0)$, where $A(t_0)$ denotes the absorbance at the initial time. [36] With the volatilization of the solvent, a general decline in relative absorbance intensity across most bands was observed (**Fig. 3c** and **S8c**). Particularly noteworthy are discernible variations in specific peaks, such as anomalous increased in relative absorbance, which serve as significant indicators of potential formation of new coordination bonds. Examination of the relative absorbance curves indicated a general decline in intensity within the spectral range of approximately 1400-1100 cm^{-1} during the coordination process. However, there were subtle increases in intensity observed near the central wavelengths at ~1365 cm^{-1} and 1255 cm^{-1}, which were attributed to the stretching vibrations of the C-N bond. Additionally, a subtle increase in intensity was noted at ~1130 cm^{-1} after crystal precipitation, attributed to the bending vibration of the N-H bond.

Subsequent to complexation completion, with the further evaporating of DMF, the complex product $(DMF)_2BMPbBr_3$ began to decomplex, pushing the central position of the C=O stretching vibrational band reverted from 1639 cm^{-1} to the longer wavenumber of 1646 cm^{-1} (**Fig. 4a**). The colorless $(DMF)_2BMPbBr_3$ crystal gradually decomplexed into yellow BM_2PbBr_4 perovskite crystal, as shown in **Fig. S9**. During DMF evaporation, the intensity of the C=O stretching vibrational band diminishes solely when the intermediate phase formation is suppressed, with no obvious shift in wavenumber position. Simultaneously, an abrupt change in intensity appeared on the same time scale, as indicated in **Fig. 4b**. This is attributed to the solution reaching its saturated solubility, prompting crystallization of BM_2PbBr_4 by direct reaction of $BMBr_2$ and $PbBr_2$, rather than gradual release of $(DMF)_2BMPbBr_3$ intermediate-phase to BM_2PbBr_4. The relative absorbance change trend of the C=O bond at different moments was extracted, revealing that the black fitting line encompassing the $(DMF)_2BMPbBr_3$ intermediate-phase exhibited a more gradual relative absorbance change at the initial stage (**Fig. S10**). The variation of the vibrational frequency of the C=O bond stands out as a pivotal indicator for discerning the presence of intermediate-phases, offering a pronounced distinction within the operando IR-FEWS spectra for the intermediate-phase evolution.

Furthermore, phenomena such as vibration band broadening and the emergence of vibration bands were discerned within the spectral bands of 1350 cm^{-1}-1400 cm^{-1} and 1120 cm^{-1}-1190 cm^{-1}. The vibration bands at 1389 cm^{-1} and 1365 cm^{-1} corresponded to the stretching vibration of the C-N bond, presented in both DMF and BM.[37,38] Initially, the absorption peak position and absorbance value of the C-N bond were primarily influenced by the presence of DMF monomers and DMF-BM hydrogen-bonded complexes in the solution. Subsequently, due to continuous DMF evaporation, hydrogen bonds between DMF and BM were broken, leading to the emergence of the vibration band of BM monomer's C-N bond II (1365 cm^{-1}). Furthermore, since both vibration bands at 1389 cm^{-1} and 1365 cm^{-1} pertain to vibration bands of the C-N bond, this also induced a slight broadening of the absorption vibration bands at the onset of evaporation. This broadening phenomenon persisted throughout the entire process of DMF monomer evaporation until the vibration band of C-N bond I at 1389 cm^{-1} completely vanished. Additionally, a series of minor vibration bands between 1190 cm^{-1} and 1130 cm^{-1} were attributed to the bending vibration of N-H bonds.[38] The N-H bonds are exclusively found in the BM

molecules. The disruption of hydrogen bonds between DMF and BM induces alterations in the bending vibration frequencies of the N-H monomers, resulting in the appearance of minor vibration bands, which are centered at 1159 cm^{-1} and 1132 cm^{-1}. It was noteworthy that presently, our infrared spectrometer possessed a time resolution averaging 32 scans per minute. Further increasing the time resolution of the infrared spectrometer, for instance, to the millisecond level, would extend to real-time monitoring of highly unstable intermediate-phase evolution in perovskite crystallization.

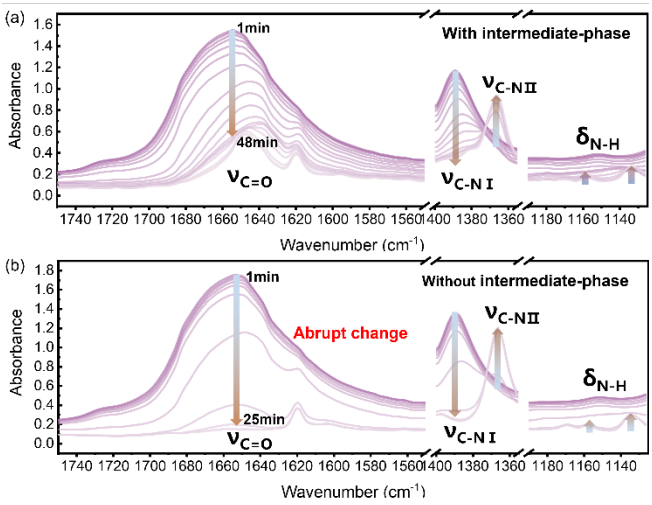

Fig. 4. Localized amplification of operando IR-FEWS spectra at 1550-1750 cm^{-1}, 1350-1400 cm^{-1}, and 1120-1190 cm^{-1} during the perovskite crystallization process. (a) Localized operando IR-FEWS spectra with the involvement of intermediate phase and (b) without the involvement of intermediate phase.

In summary, an operando infrared FEWS sensor relying on chalcogenide fibers was raised for monitoring the evolution of intermediate-phase during perovskite crystallization. The sensitivity and stability of the GAST optical fiber for monitoring various common solvents or additives was demonstrated. The shift of the stretching vibration of carbonyl groups from 1655 to 1639 cm^{-1} clearly proved the complexion of Pb^{2+} and carbonyl groups, *i.e.* the formation of $(DMF)_2BMPbBr_3$ intermediate-phase. Then the stretching vibration of carbonyl groups shifted towards original position with the intermediate-phase $(DMF)_2BMPbBr_3$ decomplexing into BM_2PbBr_4 perovskite crystal. Moreover, the broadening and anomalous emergence of new vibrational bands associating with -C-N and -N-H bonds suggest the variation of DMF-BMBr hydrogen bonds during perovskite crystallizing. Through evanescent wave infrared spectroscopy demonstration using GAST fibers, the intermediate-phase evolution was operando monitored accurately, offering valuable insights into the control of perovskite crystallization process.

Funding. National Natural Science Foundation of China (62475201, U2330115, 62275206, 61975156); State Key Laboratory of Luminescent Materials and Devices (2023-skllmd-07); Fundamental Research Funds for the Central Universities (WUT: 20231VA018).

Disclosures. The authors declare no conflicts of interest.

Data availability. Data underlying the results presented in this paper may be obtained from the authors.

Supplemental document. See Supplement 1 for supporting content.

REFERENCES

1. D.X. Ma, K.B. Lin, Y.T. Dong, et al., Nature **599**, 594 (2021).
2. C.W. Li, X.M. Wang, E.B. Bi, et al., Science **379**, 690 (2023).
3. Y. Zhou, C.B. Fei, M.A. Uddin, et al., Nature **616**, 712 (2023).
4. P. Holzhey, M. Prettl, S. Collavini, et al., Joule **7**, 257 (2023).
5. R.H. Wang, J.W. Zhu, J.Y. You, et al., Energy Environ. Sci. **17**, 2662 (2024).
6. J.Z. Jiang, M. Xiong, K. Fan, et al., Nat. Photonics **16**, 575 (2022).
7. X. Li, C. Liu, F. Ding, et al., Adv. Funct. Mater. **33**, 2213360 (2023).
8. R.D.J. Oliver, P. Caprioglio, F. Peña-Camargo, et al., Energy Environ. Sci. **15**, 714 (2022).
9. W.Z. Xu, Y. Gao, W.J. Ming, et al., Adv. Mater. **32**, 2003965 (2020).
10. Y. Liu, X.P. Zheng, Y.J. Fang, et al., Nat. Commun. **12**, 8 (2021).
11. L. Ma, Z.G. Yan, X.Y. Zhou, et al., Nat. Commun. **12**, 10 (2021).
12. F. Yao, J.L. Peng, R.M. Li, et al., Nat. Commun. **11**, 9 (2020).
13. M.C. Qin, K.F. Tse, T.K. Lau, et al., Adv. Mater. **31**, 1901284 (2019).
14. H.B. Ran, T. Ouyang, S.Y. Wang, et al., J. Mater. Chem. C **11**, 11529 (2023).
15. H.H. Ding, K.R. Yan, B.R. Li, et al., Adv. Mater. Interfaces **8**, 2100120 (2021).
16. P.E. Marchezi, E.M. Therézio, R. Szostak, et al., J. Mater. Chem. A **8**, 9302 (2020).
17. W.C. Lin, W.C. Lo, J.X. Li, et al., Npj Mater. Degrad. **5**, 13 (2021).
18. H. Funk, O. Shargaieva, A. Eljarrat, et al., J. Phys. Chem. Lett. **11**, 4945 (2020).
19. J.J. Van Franeker, K.H. Hendriks, B.J. Bruijnaers, et al., Adv. Energy Mater. **7**, 1601822 (2017).
20. E. Serpetzoglou, I. Konidakis, T. Maksudov, et al., J. Mater. Chem. C **7**, 12170 (2019).
21. D.V. Athapaththu, M.E. Kordesch, and J.X. Chen, J. Phys. Chem. Lett. **15**, 1105 (2024).
22. R. Szostak, A.D. Gonçalves, J.N.D. Freitas, et al., Chem. Rev. **123**, 3160 (2023).
23. B.C. He, C.Y. Wang, J.L. Li, et al., Nanomaterials **13**, 1983 (2023).
24. M.Q. Liao, M.L. Xia, Y.S. Xu, et al., Chem. Commun. **59**, 8758 (2023).
25. C.P. Grey, and J.M. Tarascon, Nat. Mater. **16**, 45 (2017).
26. J.Q. Huang, S.T. Boles, and J.M. Tarascon, Nat. Sustain. **5**, 194 (2022).
27. J. Peng, X. Zhou, S.H. Jia, et al., J. Power Sources **433**, 226692 (2019).
28. A. Raghavan, P. Kiesel, L.W. Sommer, et al., J. Power Sources **341**, 466 (2017).
29. B.Y. Xia, J.J. Jin, N. Wang, et al., Adv. Funct. Mater. **34**, 2308581 (2024).
30. J.Q. Huang, X.L. Han, F. Liu, et al., Energy Environ. Sci. **14**, 6464 (2021).
31. Z.J. Li, Y.K. Zhao, and T.X. You, Sensors **23**, 4841 (2023).
32. Y.K. Zhao, X.D. Zhao, and Z.J. Li, Sensor Actuat B-Chem **405**, 135361 (2024).
33. L. Calvez, Comptes Rendus Phys. **18**, 314 (2017).
34. P. Fomina, A. Femenias, M. Hlavatsch, et al., Appl. Spectrosc. **77**, 1073 (2023).
35. X.J. Sun, M.L. Xia, M.Q. Liao, et al., Cryst. Growth Des. **23**, 3632 (2023).
36. C. Gervillié-Mouravieff, C. Boussard-Plédel, J.Q. Huang, et al., Nat. Energy **7**, 1157 (2022).
37. M. Saldyka, Z. Mielke, and K. Haupa, Spectrochim. Acta A **190**, 423 (2018).
38. V. Arjunan, A. Raj, P. Ravindran, et al., Spectrochim. Acta A **118**, 951 (2014).

REFERENCES

1. D.X. Ma, K.B. Lin, Y.T. Dong, et al., Distribution control enables efficient reduced-dimensional perovskite LEDs. Nature **599**, 594 (2021).
2. C.W. Li, X.M. Wang, E.B. Bi, et al., Rational design of Lewis base molecules for stable and efficient inverted perovskite solar cells. Science **379**, 690 (2023).
3. Y. Zhou, C.B. Fei, M.A. Uddin, et al., Self-powered perovskite photon-counting detectors. Nature **616**, 712 (2023).
4. P. Holzhey, M. Prettl, S. Collavini, et al., Toward commercialization with lightweight, flexible perovskite solar cells for residential photovoltaics. Joule **7**, 257 (2023).
5. R.H. Wang, J.W. Zhu, J.Y. You, et al., Custom-tailored solvent engineering for efficient wide-bandgap perovskite solar cells with a wide processing window and low VOC losses. Energy Environ. Sci. **17**, 2662 (2024).
6. J.Z. Jiang, M. Xiong, K. Fan, et al., Synergistic strain engineering of perovskite single crystals for highly stable and sensitive X-ray detectors with low-bias imaging and monitoring. Nat. Photonics **16**, 575 (2022).
7. X. Li, C. Liu, F. Ding, et al., Ultra-stable and sensitive ultraviolet photodetectors based on monocrystalline perovskite thin films. Adv. Funct. Mater. **33**, 2213360 (2023).
8. R.D.J. Oliver, P. Caprioglio, F. Peña-Camargo, et al., Understanding and suppressing non-radiative losses in methylammonium-free wide-bandgap perovskite solar cells. Energy Environ. Sci. **15**, 714 (2022).
9. W.Z. Xu, Y. Gao, W.J. Ming, et al., Suppressing defects-induced nonradiative recombination for efficient perovskite solar cells through green antisolvent engineering. Adv. Mater. **32**, 2003965 (2020).
10. Y. Liu, X.P. Zheng, Y.J. Fang, et al., Ligand assisted growth of perovskite single crystals with low defect density. Nat. Commun. **12**, 8 (2021).
11. L. Ma, Z.G. Yan, X.Y. Zhou, et al., A polymer controlled nucleation route towards the generalized growth of organic-inorganic perovskite single crystals. Nat. Commun. **12**, 10 (2021).
12. F. Yao, J.L. Peng, R.M. Li, et al., Room-temperature liquid diffused separation induced crystallization for high-quality perovskite single crystals. Nat. Commun. **11**, 9 (2020).
13. M.C. Qin, K.F. Tse, T.K. Lau, et al., Manipulating the mixed-perovskite crystallization pathway unveiled by in situ GIWAXS. Adv. Mater. **31**, 1901284 (2019).
14. H.B. Ran, T. Ouyang, S.Y. Wang, et al., Rational design of the synergistic effect with lead iodide as the link for improving the efficiency of carbon-based perovskite solar cells. J. Mater. Chem. C **11**, 11529 (2023).
15. H.H. Ding, K.R. Yan, B.R. Li, et al., In situ investigation of the $Cu/CH_3NH_3PbI_3$ interface in perovskite device. Adv. Mater. Interfaces **8**, 2100120 (2021).
16. P.E. Marchezi, E.M. Therézio, R. Szostak, et al., Degradation mechanisms in mixed-cation and mixed-halide $Cs_xFA_{1-x}Pb(Br_yI_{1-y})_3$ perovskite films under ambient conditions. J. Mater. Chem. A **8**, 9302 (2020).
17. W.C. Lin, W.C. Lo, J.X. Li, et al., In situ XPS investigation of the X-ray-triggered decomposition of perovskites in ultrahigh vacuum condition. Npj Mater. Degrad. **5**, 13 (2021).
18. H. Funk, O. Shargaieva, A. Eljarrat, et al., In situ TEM monitoring of phase-segregation in inorganic mixed halide perovskite. J. Phys. Chem. Lett. **11**, 4945 (2020).
19. J.J. Van Franeker, K.H. Hendriks, B.J. Bruijnaers, et al., Monitoring thermal annealing of perovskite solar cells with in situ photoluminescence. Adv. Energy Mater. **7**, 1601822 (2017).
20. E. Serpetzoglou, I. Konidakis, T. Maksudov, et al., In situ monitoring of the charge carrier dynamics of CH3NH3PbI3 perovskite crystallization process. J. Mater. Chem. C **7**, 12170 (2019).
21. D.V. Athapaththu, M.E. Kordesch, and J.X. Chen, Monitoring phase separation and dark recovery in mixed halide perovskite clusters and single crystals using in situ spectromicroscopy. J. Phys. Chem. Lett. **15**, 1105 (2024).
22. R. Szostak, A.D. Gonçalves, J.N.D. Freitas, et al., In situ and operando characterizations of metal halide perovskite and solar cells: insights from lab-sized devices to upscaling processes Chem. Rev. **123**, 3160 (2023).
23. B.C. He, C.Y. Wang, J.L. Li, et al., In situ and operando characterization techniques in stability study of perovskite-based devices. Nanomaterials **13**, 1983 (2023).
24. M.Q. Liao, M.L. Xia, Y.S. Xu, et al., Growth mechanism of metal halide perovskite single crystals in solution. Chem. Commun. **59**, 8758 (2023).
25. C.P. Grey, and J.M. Tarascon, Sustainability and in situ monitoring in battery development. Nat. Mater. **16**, 45 (2017).
26. J.Q. Huang, S.T. Boles, and J.M. Tarascon, Sensing as the key to battery lifetime and sustainability. Nat. Sustain. **5**, 194 (2022).
27. J. Peng, X. Zhou, S.H. Jia, et al., High precision strain monitoring for lithium ion batteries based on fiber Bragg grating sensors. J. Power Sources **433**, 226692 (2019).
28. A. Raghavan, P. Kiesel, L.W. Sommer, et al., Embedded fiber-optic sensing for accurate internal monitoring of cell state in advanced battery management systems part 1: Cell embedding method and performance. J. Power Sources **341**, 466 (2017).
29. B.Y. Xia, J.J. Jin, N. Wang, et al., Degradation evolution of perovskite solar cells via in situ real-time optical observation. Adv. Funct. Mater. **34**, 2308581 (2024).
30. J.Q. Huang, X.L. Han, F. Liu, et al., Monitoring battery electrolyte chemistry via in-operando tilted fiber Bragg grating sensors. Energy Environ. Sci. **14**, 6464 (2021).
31. Z.J. Li, Y.K. Zhao, and T.X. You, Infrared evanescent wave sensing based on a Ge10As30Se40Te20 fiber for alcohol detection. Sensors **23**, 4841 (2023).
32. Y.K. Zhao, X.D. Zhao, and Z.J. Li, Infrared tapered fiber ring sensor for environmental detection of organic pollutants. Sensor Actuat B-Chem **405**, 135361 (2024).
33. L. Calvez, Chalcogenide glasses and glass-ceramics: Transparent materials in the infrared for dual applications. Comptes Rendus Phys. **18**, 314 (2017).
34. P. Fomina, A. Femenias, M. Hlavatsch, et al., A portable infrared attenuated total reflection spectrometer for food analysis. Appl. Spectrosc. **77**, 1073 (2023).
35. X.J. Sun, M.L. Xia, M.Q. Liao, et al., Controllable Synthesis of Centimeter-Sized 2D Ruddlesden-Popper Perovskite Single Crystals through Intermediate-Phase Engineering. Cryst. Growth Des. **23**, 3632 (2023).
36. C. Gervillié-Mouravieff, C. Boussard-Plédel, J.Q. Huang, et al., Unlocking cell chemistry evolution with operando fibre optic infrared spectroscopy in commercial Na(Li)-ion batteries. Nat. Energy **7**, 1157 (2022).
37. M. Saldyka, Z. Mielke, and K. Haupa, Structural and spectroscopic characterization of DMF complexes with nitrogen, carbon dioxide, ammonia and water. Infrared matrix isolation and theoretical studies. Spectrochim. Acta A **190**, 423 (2018).
38. V. Arjunan, A. Raj, P. Ravindran, et al., Structure-activity relations of 2-(methylthio)benzimidazole by FTIR, FT-Raman, NMR, DFT and conceptual DFT methods. Spectrochim. Acta A **118**, 951 (2014).